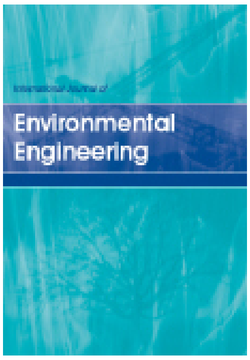

International Journal of Environmental Engineering

ISSN online: 1756-8471 - ISSN print: 1756-8463
https://www.inderscience.com/ijee

Temporal and spatial pattern of vegetation community diversity in Henan section of the Yellow River Basin based on remote sensing and ecological model

Yingchun Pei, Xiaolei Zhang, Yening Wang

DOI: 10.1504/IJEE.2026.10079892

Article History:

Received:	15 October 2025
Last revised:	05 February 2026
Accepted:	05 February 2026
Published online:	21 July 2026

Temporal and spatial pattern of vegetation community diversity in Henan section of the Yellow River Basin based on remote sensing and ecological model

Yingchun Pei, Xiaolei Zhang and Yening Wang*

Institute of Geographical Sciences,
Henan Academy of Sciences,
Zhengzhou, Henan, 450052, China
Email: peiyingchun104@163.com
Email: skyxlzhang@126.com
Email: ynwang@igs-has.cn
*Corresponding author

Abstract: Henan section of the Yellow River Basin lies in transition zone between warm-temperate and northern subtropical zones. Its vegetation communities exhibit significant spatial and temporal heterogeneity under combined influence of climate change and land-use transformation. This study used MaxEnt species distribution model and community land model (CLM) ecosystem process model to analyse temporal and spatial evolution laws and driving mechanisms of vegetation community diversity in Henan section. The results showed that the vegetation coverage (mean NDVI) showed an overall upward trend, however, the spatial differentiation was clear. Human activity intensity index was significantly negatively correlated with vegetation diversity. Climatic factors have the strongest influence on the variation of vegetation patterns. Furthermore, vegetation diversity was more strongly affected by autumn temperature fluctuations. By this study, nonlinear effects of multiscale environmental factors on vegetation communities are revealed, providing a quantitative basis for ecological protection and restoration in the Yellow River Basin.

Keywords: Henan section of the Yellow River Basin; vegetation community diversity; remote sensing monitoring; ecological models; spatiotemporal pattern.

Reference to this paper should be made as follows: Pei, Y., Zhang, X. and Wang, Y. (2026) 'Temporal and spatial pattern of vegetation community diversity in Henan section of the Yellow River Basin based on remote sensing and ecological model', *Int. J. Environmental Engineering*, Vol. 14, No. 6, pp.1–24.

Biographical notes: Yingchun Pei received her PhD degree from School of Life Sciences, Henan University in 2021. She is an assistant researcher in the Institute of Geographical Sciences, Henan Academy of Sciences, Zhengzhou, China. She has published over ten papers in various journals and is responsible for four research projects. Her research interests include community ecology, ecosystem restoration and ecological security.

Xiaolei Zhang received his PhD from Institute of Environment and Engineering in Cold and Dry Areas, Chinese Academy of Sciences in 2010. He is an associate researcher in the Institute of Geographical Sciences, Henan Academy of Sciences, Zhengzhou, China. He has published 60 papers in various journals and is responsible for 30 research projects. His current research interests include sustainable development of resources and environment and geographic ecology.

Yening Wang received his PhD degree from the University of Chinese Academy of Sciences in 2020. He is currently an associate researcher in the Institute of Geographical Sciences, Henan Academy of Sciences. He has published 20 papers in various journals and is responsible for 6 research projects. His research interests include sustainable development of resources and environment, landscape ecology, and urban ecology.

1 Introduction

As an important ecological transition zone in China, the Henan section of the Yellow River Basin bears unique physical and geographical features and complex man-land relationships (Bai et al., 2024; Chai et al., 2024). This area lies at the junction of the warm-temperate and northern subtropical zones. The landform types cover mountains, hills, plains, and other forms. The monsoon system and topography affect the climatic conditions, forming an ecological interface with distinct gradients. Against the backdrop of intensified climate change and the ongoing intensification of human activities, the composition, structure, and spatial distribution patterns of vegetation communities are undergoing unprecedented dynamic evolution (Bhatt and Maclean, 2023). This evolution relates to the maintenance of the service functions of regional ecosystems. It profoundly impacts key ecological processes such as soil and water conservation and carbon sink regulation (Fernandez-Guisuraga et al., 2023). Traditional ground survey methods are limited by spatial and temporal resolution, workforce, and material resources, and it is difficult to capture the continuous change characteristics of large-scale vegetation communities fully. However, combining the remote sensing technology's multi-source data acquisition ability and ecological models' spatial simulation advantages provides a new technical path for analysing vegetation diversity's spatial and temporal heterogeneity (Wilkho et al., 2025; Zavari et al., 2022).

Currently, research on vegetation dynamics in the Yellow River Basin mostly focuses on describing community characteristics at a single time point or on the isolated analysis of specific driving factors, lacking a systematic examination of the coupling effects of multiple factors across long time series. Especially in the Henan section, where human activities are intensive, the urbanisation process and the transformation of agricultural production mode have significantly changed the surface cover structure. The fluctuation of the river hydrological situation and the regulation of water conservancy projects are intertwined, forming a complex ecological stress network (Chen et al., 2023b). These factors continuously affect the succession direction of vegetation communities by changing soil moisture conditions, light resources, and interspecific competition (van Deventer et al., 2022). However, there are still cognitive gaps in existing studies on the mechanisms underlying responses to multi-scale environmental factors and vegetation dynamics, especially regarding how interactions between geomorphic units and climatic elements shape the spatial patterns of vegetation, and a complete explanatory framework has not yet been established.

The development of remote sensing technology offers opportunities to overcome the time and spatial limitations of traditional research methods (Zhang et al., 2023; Wang et al., 2025). Multi-spectral and hyperspectral sensors can capture vegetation's physiological and biochemical characteristics; radar data can penetrate clouds to obtain three-dimensional surface structure information; and the UAV platform can achieve centimetre-level accuracy in local ecological process observation. The deep coupling of these multi-source remote sensing data with ecological models makes it possible to reconstruct the spatiotemporal dynamics of vegetation communities at the landscape scale (Chen et al., 2023a). By integrating the light energy utilisation efficiency model and the species distribution model, a nonlinear response relationship between environmental gradients and biodiversity can be constructed, and the contributions of different niche factors to the formation of vegetation patterns can be revealed (Chen et al., 2024). This technology integration can improve the efficiency of large-scale ecological monitoring and help identify the driving thresholds of key ecological processes, providing a scientific basis for formulating regional ecological restoration strategies.

At the practical level, the Henan section is the core implementation area of the ecological protection and high-quality development strategy of the Yellow River Basin, and the stability of its vegetation community is directly related to the ecological security pattern of the entire basin. At present, evaluating the implementation effects of ecological construction projects urgently requires more detailed spatiotemporal dynamic data, especially after projects such as returning farmland to forests and wetland restoration. Quantifying the synergistic effect of artificial intervention and natural restoration requires establishing a scientific evaluation index system. Parameters such as vegetation coverage and leaf area index obtained by remote sensing inversion, combined with potential natural vegetation distribution simulated by the ecological model, can effectively identify the disturbance intensity of human activities on vegetation succession trajectories and provide decision support for optimising the ecological compensation mechanism (Chi et al., 2022). This multi-technology integration analysis paradigm has important practical significance for balancing regional economic development and ecological protection.

This study focuses on the Henan section of the Yellow River Basin, a typical ecologically fragile area. The collaborative modeling method of integrated species distribution model (MaxEnt) and land surface process model (CLM) is used as the core to systematically reveal the spatiotemporal evolution pattern of vegetation community diversity and its environmental driving mechanism. The study constructs a coupled analysis framework of multi-source remote sensing data and dual models to analyse the key controlling factors of vegetation pattern formation at different spatiotemporal scales, and clarify the composite impact path of climate change and human activities on ecological processes. In terms of research methods, it emphasises the results complementarity and cross validation between models, breaks through the limitations of single model in mechanism interpretation or prediction ability, and aims to explore the method innovation and efficiency improvement of multi model integration in regional ecological research. The research results are expected to provide a more reliable theoretical basis for the adaptive management of the ecosystem in the Yellow River

Basin, and provide a new technological path for vegetation dynamic monitoring and simulation in similar geographical units.

This study proposes the following core scientific hypothesis: Under the joint drive of climate change and high-intensity human activities, the spatiotemporal differentiation of vegetation diversity in the study area from 2000 to 2022 is mainly regulated by the interaction between terrain gradient and land use intensity. Specifically, due to superior natural conditions and weaker human interference, the vegetation restoration rate and species richness in the western mountainous areas will be significantly higher than those in the eastern plains dominated by cultivated land expansion and urban construction. In addition, the ecological engineering implementation area may lead to a decrease in understory community diversity due to the singularity of tree species while improving vegetation coverage. This study will quantitatively validate this hypothesis by coupling the MaxEnt species distribution model with the community land model (CLM) ecosystem process model, and combining multi-source remote sensing and ground observation data.

2 Theoretical basis for studying spatiotemporal patterns of vegetation community diversity

2.1 Theory of multi-scale heterogeneity of ecosystems

Spatial heterogeneity refers to the uneven distribution of ecosystems on small and medium scales, which is essential for biodiversity and ecological function maintenance (Dai et al., 2022; Duan et al., 2022). Figure 1 shows the spatial heterogeneity architecture of the ecosystem. It is divided into habitat heterogeneity and population heterogeneity. Habitat heterogeneity involves the spatial distribution of different habitats, and population heterogeneity focuses on the distribution of individuals of the same species in different locations.

Figure 1 Spatial heterogeneity architecture of ecosystem (see online version for colours)

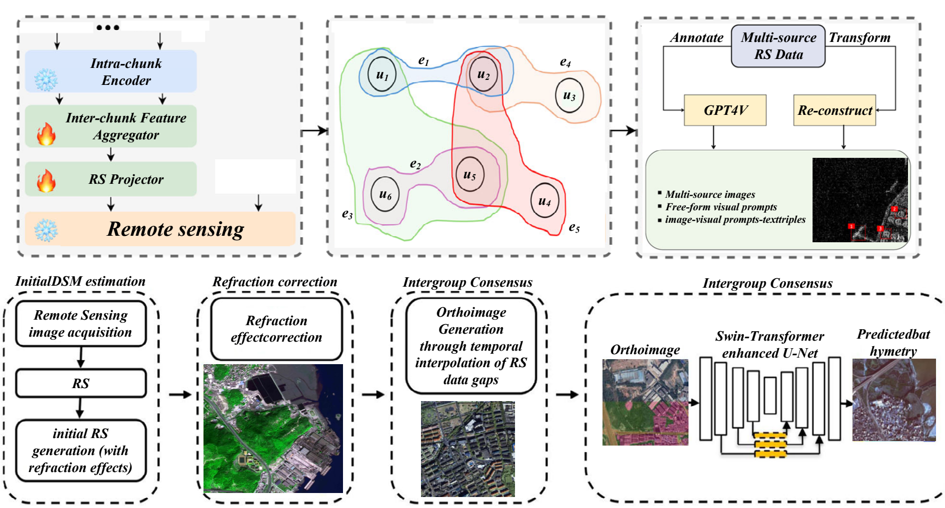

Spatial heterogeneity is influenced by both natural and anthropogenic factors, including topography, soil, climate, land use, urban expansion and agricultural activities (Han et al., 2024). It has a significant impact on ecosystem functions, improves species diversity, affects material cycles and energy flows, and enhances the ecosystem's ability to resist disturbances. In ecosystem management, maintaining and promoting spatial heterogeneity is the key strategy, involving the protection of critical habitats, restoration of damaged ecosystems, and rational land use to maintain biodiversity and ecosystem health (Hou et al., 2024; Muentes et al., 2024).

Spatial heterogeneity of ecosystems is commonly studied using remote sensing techniques, GIS, and ground surveys to understand their distribution, causes, and ecological impacts (Sharma, 2022). Spatial heterogeneity is crucial to ecosystem diversity and function, and therefore, its recognition and conservation are central to ecosystem management.

The human activity intensity index selects four core indicators: land use intensity (construction land and cultivated land expansion), traffic interference (weighted road density), population pressure (population density), and nighttime light intensity. All data are standardised to a spatial resolution of 1km and weighted using a combination of subjective and objective weighting methods. The entropy weight method (objective) is combined with the Analytic Hierarchy Process to determine the weight ratios of construction land density (0.28), cultivated land expansion intensity (0.22), road density (0.20), population density (0.18), and nighttime light intensity (0.12).

2.2 Synergistic mechanism of remote sensing and ecological model coupling

The imaging principle of remote sensing images is complex, and it is affected by differences in satellite platforms, sensors, and changes in time series data acquisition. This results in significant differences in spatial, spectral, and temporal dimensions (Tang et al., 2022).

Used Landsat and MODIS multi-source remote sensing data to construct a data fusion framework with complementary spatiotemporal resolution. The specific selection principle is as follows: Landsat data provides high-resolution surface coverage details for finely characterising the spatial heterogeneity of vegetation communities; MODIS data, with its high temporal resolution advantage, effectively captures vegetation phenological dynamics and seasonal changes. In terms of data fusion processing, the Spatiotemporal Adaptive Fusion Algorithm (STARFM) is used to fuse the high temporal frequency information of MODIS with the high spatial details of Landsat, generating a spatially and temporally continuous high-resolution NDVI sequence (30 metre resolution). This not only overcomes the limitations of a single data source in terms of spatiotemporal resolution, but also ensures the consistency of long-term series data. Meanwhile, through strict atmospheric correction, geometric registration, and radiometric calibration preprocessing, the comparability of multi-source data in the same coordinate system and radiometric reference is ensured, providing reliable input parameters for subsequent ecological model simulations.

In the MaxEnt model, a vegetation distribution dataset was constructed based on field surveys and literature data. Multiple environmental variables such as terrain, climate, soil, and human activities were combined, and the model was trained through feature combination optimisation, regularisation coefficient tuning (0.5–4.0), and 10 fold cross validation. Performance was evaluated using indicators such as AUC and TSS, and all parameters and random seeds were fixed and recorded. The CLM model is initialised based on regional meteorological forcing data, vegetation parameters and soil attributes retrieved from remote sensing. By calibrating vegetation physiological parameters and soil carbon cycling parameters in stages, the simulated leaf area index, total primary productivity are matched with remote sensing products and ground observations, and the GLUE method is used for parameter optimisation.

The spatial resolution of remote sensing images is one of the key characteristics, which determines the sensor's ability to distinguish adjacent objects. The spatial resolution reflects the size of the area over which the pixels cover the ground (Wang et al., 2023; Zhu et al., 2024). High resolution means that the image is more finely detailed, helping to accurately depict ground features such as buildings, farmland, and the ocean. In addition, high-resolution remote sensing images also provide richer information for urban planning, agricultural monitoring and marine environment observation.

The spectral range of a sensor determines its ability to capture electromagnetic waves, including visible light, infrared light, and ultraviolet light, among others (Qin et al. 2023; Shi et al. 2023). This range is essential for remote sensing images to distinguish feature categories like vegetation and soil types. Remote sensing images with wide spectral range have irreplaceable value in agriculture, environmental protection and geological exploration.

The revisiting period is the shortest interval between two consecutive detections of the same place by sensors, reflecting the acquisition and update speed of remote sensing information. A shorter revisit cycle means more frequent monitoring of specific areas, crucial to tracking dynamic changes such as seasonal disasters, urban traffic flows, etc. To construct the reduced-resolution dataset and reference image, we need to follow the Wald protocol and follow the following steps: First, the original PAN and MS images are processed with a low-pass filter to adapt them to the satellite sensor MTF. Then, the filtered image is spatially degraded, and the degradation coefficient is based on the resolution ratio of the PAN and MS images. Finally, the degraded PAN and MS images form a reduced-resolution dataset, and the unprocessed MS images serve as reference images.

The criteria for reference quality assessment usually include spatial correlation coefficient (SCC), spectral angle mapping (SAM), relative global error (ERGAS), structural similarity measure (SSIM), and universal image quality indicator (UIQI), among others (Zhao et al., 2022; Ci et al., 2024). These indicators are defined and calculated as follows:

The *SCC* evaluates the spatial detail preservation of the fused images, and the calculation is divided into two steps (Cui et al., 2024). First, a high-pass filter extracts the high-frequency information of the fused image and the reference image. A commonly used one is a Laplace mask, and its expression is shown in equation (1).

$$Lap = \begin{bmatrix} -1 & -1 & -1 \\ -1 & 8 & -1 \\ -1 & -1 & -1 \end{bmatrix} \tag{1}$$

Here *Lap* refers to the Laplacian operator. According to formula (2), calculate the high-frequency information correlation coefficient *SCC* of the two smoothed images:

$$SCC(F,R)=\frac{\sigma_{fr}}{\sigma_f\sigma_r} \tag{2}$$

F and *R* represent the fused image and the reference image, respectively, σ_f and σ_r are their standard deviations, and σ_{fr} is the covariance between them. The *SCC* value range is –1 to 1. The larger the SCC value, the stronger the spatial information correlation between the fused image and the reference image, and the better the spatial quality. The SAM indicator evaluates the spectral distortion of the fused image versus the reference image (Feng et al., 2023a). SAM regards each spectral band as a coordinate axis, converts pixels into spectral vectors, and calculates the angle between the two vectors to determine the degree of spectral distortion. The calculation formula is shown in equation (3):

$$SAM\left(F_{\{i\}},R_{\{i\}}\right)=\arccos\left(\frac{F_{\{i\}},R_{\{i\}}}{\left\|F_{\{i\}}\right\|\cdot\left\|R_{\{i\}}\right\|}\right) \tag{3}$$

In a multispectral image, the spectral vector of pixel point *n* is expressed as $F/R_{\{n\}} = \{F/R_{1,\{n\}},\ldots, F/R_{k,\{n\}}\}$, where *F* is the fused image, *R* is the reference image, and *K* is the number of bands. The vector inner product is represented by $<\cdot,\cdot>$ and the *L2* norm is represented by $||\cdot||$. The *SAM* value is the calculated average of all pixels, and the ideal value is 0. The *ERGAS* metric evaluates the overall distortion degree of the fused image from the reference image, based on *RMSE*, with an ideal value of 0 indicating a perfect match. The calculation method is shown in the following equations (4) to (5):

$$ERGAS(F,R)=100\frac{h}{l}\sqrt{\frac{1}{N}\sum_{i=1}^{\mathrm{N}}\left(\frac{RMSE\left(F_{\mathrm{i}},R_{\mathrm{i}}\right)}{\mu\left(R_{\mathrm{i}}\right)}\right)^2} \tag{4}$$

$$RMSE(F,R)=\sqrt{\frac{1}{N}\sum_{i=1}^{N}\left(F_{\mathrm{i}}-R_{\mathrm{i}}\right)^2} \tag{5}$$

F and *R* represent the fused image and the reference image, respectively, *h* and *l* represent the initial spatial resolution of the PAN image and the MS image, *i* is the band index, *N* is the total number of bands, and μ is the pixel average. The *SSIM* index evaluates the structural similarity between the fused image and the reference image, and its calculation formula (6) is as follows:

$$SSIM(F,R)=\frac{\left(2\mu_f\mu_r+\mathrm{c}_1\right)\left(2\sigma_{fr}+\mathrm{c}_2\right)}{\left(\mu_f^2+\mu_r^2+\mathrm{c}_1\right)\left(\sigma_f^2+\sigma_r^2+\mathrm{c}_2\right)} \tag{6}$$

F and *R* represent the fused image and the reference image, respectively, μ_f and μ_r are their mean values, and c_1 and c_2 are constant terms. σ_f and σ_r are the standard deviations and σ_{fr} is the covariance. SSIM values close to 1 indicate high structural similarity. The UIQI indicator, the Q index, evaluates the similarity of structural information between the fused image and the reference image in terms of correlation, brightness, and contrast

(Feng and Qu 2023). The value range is –1 to 1. The larger the value, the higher the similarity. See equation (7) for the calculation method.

$$Q(F,R)=\frac{4\sigma_{fr}\mu_f\mu_r}{\left(\sigma_f^2+\sigma_r^2\right)\left(\mu_f^2+\mu_r^2\right)} \tag{7}$$

F and *R* represent the fused image and the reference image, respectively, μ_f and μ_r are their mean values, σ_f and σ_r are their standard deviations, and σ_{fr} is their covariance. In remote sensing image fusion, the *Q* index can be expanded to the Q_4 index of four channels, and each pixel $I_{\{i\}}$ is constructed as a quadruple. The calculation method is shown in formula (8).

$$I_{\{i\}}=I_{\{i\},1}+\alpha I_{\{i\},2}+\beta I_{\{i\},3}+\gamma I_{\{i\},4} \tag{8}$$

Equation (9) calculates the Q_4 index of the 4-channel fused image and the reference image by using the preset channel weight coefficients α, β and γ.

$$Q_4=Q\left(F_{\{i\}},R_{\{i\}}\right) \tag{9}$$

In this study, the multi-channel quality assessment index Q_{2n} index was developed to evaluate remote sensing image fusion tasks with more than four channels. In the study, the evaluation indexes are selected according to the characteristics of the data set, and UIQI identification is uniformly used. The reduced resolution data set and image are constructed by Wald protocol with reference to the evaluation index, and the fused image is evaluated. However, these rely on the evaluation index and scale invariance assumption of Wald protocol, assuming that the fusion model performs consistently on different resolution datasets.

Figure 2 Integrated workflow of remote sensing and ecological model coupling framework (see online version for colours)

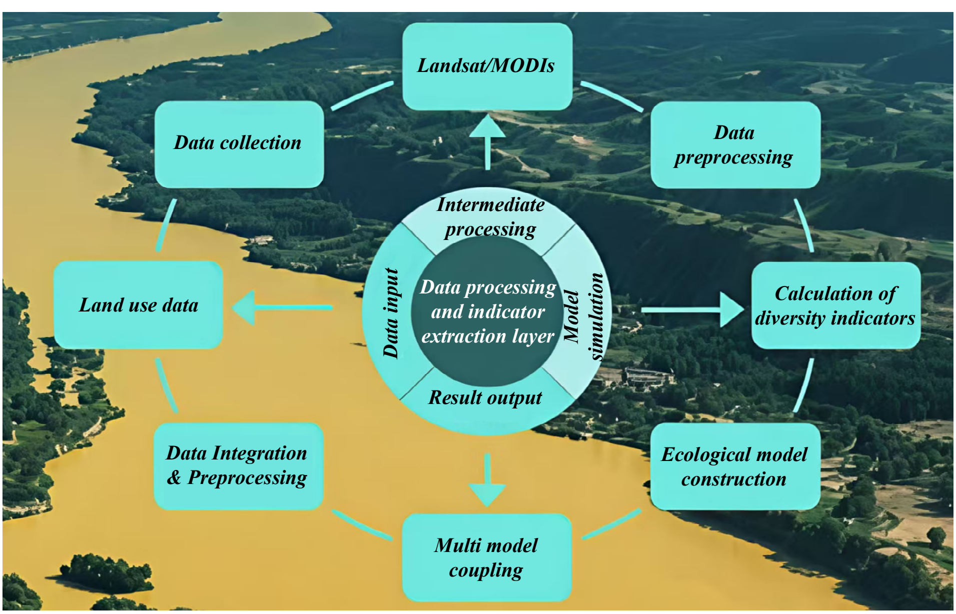

The workflow in Figure 2 reflects the closed-loop research paradigm of 'data model validation'. Multi source remote sensing data provides a large-scale, long-term observation basis, ecological models reveal the mechanism of pattern formation, and ground validation data ensures the reliability of results. The entire framework is applicable to vegetation ecological research in mesoscale heterogeneous regions such as the Henan section of the Yellow River Basin, and can provide methodological support for regional ecological restoration assessment.

3 Construction of spatiotemporal vegetation model in Henan section of Yellow River Basin

3.1 Model integration framework for multi-source data coupling

Geodetector is a statistical model used to study the difference in spatial distribution. It can quantitatively identify the influence of a single factor, the interaction strength of two factors and the risk areas. This method does not rely on linear assumptions, can accurately explain the interaction between factors, and effectively analyses the relationship between vegetation and driving factors (Feng et al., 2023b). Figure 3 shows the model integration framework of multi-source data fusion. The geographic detector can be used to quantitatively analyse the spatial distribution characteristics and driving factors of vegetation NDVI change in the Yellow River region, including four main parts: differentiation and factor detection, interaction detection, risk area detection and ecological detection.

Figure 3 Model integration framework for multi-source data coupling (see online version for colours)

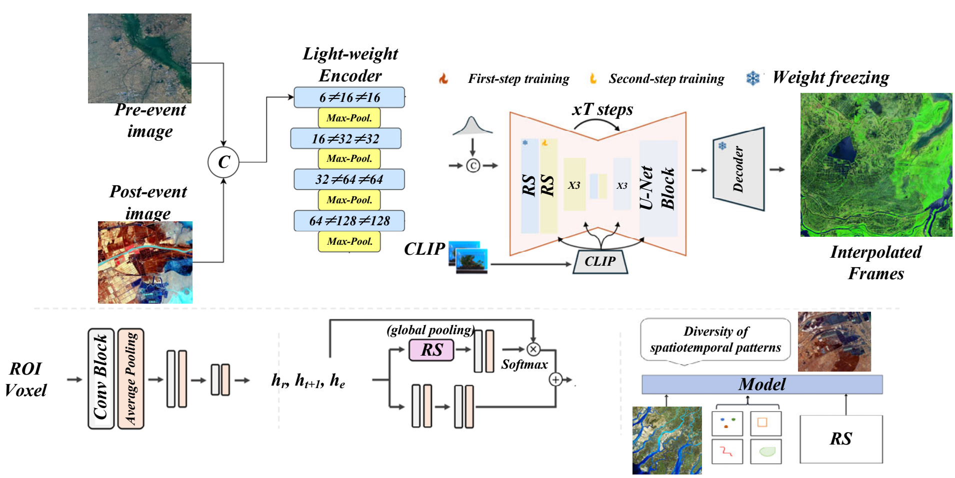

Detection difference and factor analysis aims to study the difference in spatial distribution of dependent variable Y and the influence of its driving factors. The formulas for calculating the value of factor explanatory power q are (10) to (11).

$$q = 1 - \frac{\sum_{h=1}^{L} N_h \sigma_h^2}{N\sigma^2} = 1 - \frac{SSW}{SST} \tag{10}$$

$$SSW = \sum_{h=1}^{L} N_h \sigma_h^2 \quad SST = N\sigma^2 \tag{11}$$

In the formula, q represents the ability of independent variable X to explain the spatial difference of dependent variable Y. The detector divides the study area into $h = 1$ to L sub-regions, that is, classifies or segments. N_h and N are the total number of units for a specific layer h and the whole region, and $\sigma^2{}_h$ and σ^2 are the variance of layer h from the value of the dependent variable Y for the whole region. SSW and SST represent the sum of sub-region variance and the total variance of the whole region, respectively.

Probing interactions aims to identify the interactions between drivers and evaluate their impact on the ability to explain differences in the spatial distribution of dependent variables. By calculating the explanatory power of individual factors and their interactions, these values are compared to determine the interactions between factors. Probing risk areas aims to assess whether the drivers differ significantly in attribute mean values within sub-areas to look for places with high vegetation cover. The test was performed using the t-statistic as shown in equation (12).

$$t_{\bar{y}_{h=1} - \bar{y}_{h=2}} = \frac{\bar{Y}_{h=1} - \bar{Y}_{h=2}}{\left[\frac{Var\left(\bar{Y}_{h=1}\right)}{n_{h=1}} + \frac{Var\left(\bar{Y}_{h=2}\right)}{n_{h=2}} \right]^{\frac{1}{2}}} \tag{12}$$

In the formula, $\bar{Y}_h$ represents the mean value of attributes in sub-region h, such as NDVI or vegetation coverage, n_h is the number of samples in sub-region h, and Var represents the variance. The statistic t approximately follows the Student's t distribution, and its degrees of freedom are calculated according to equation (13).

$$df = \frac{\frac{Var\left(\bar{Y}_{h=1}\right)}{n_{h=1}} + \frac{Var\left(\bar{Y}_{h=2}\right)}{n_{h=2}}}{\frac{1}{n_{h=1} - 1}\left[\frac{Var\left(\bar{Y}_{h=1}\right)}{n_{h=1}} \right]^2 + \frac{1}{n_{h=2} - 1}\left[\frac{Var\left(\bar{Y}_{h=2}\right)}{n_{h=2}} \right]^2} \tag{13}$$

Assuming zero $\bar{Y}_{h=1} = \bar{Y}_{h=2}$. If it is rejected at the confidence level α, it means that the attribute mean values of the two sub-regions are significantly different. Ecological detection evaluates whether the effects of the two driving factors X_1 and X_2 on the dependent variable Y are significantly different. For example, it determines the difference in the effects of X_1 and X_2 on the spatial distribution of vegetation coverage, and uses statistics to evaluate the significance of the difference. See formulas (14) to (15) for details.

$$F = \frac{N_{X_1}\left(N_{X_2} - 1\right) SSW_{X_2}}{N_{X_2}\left(N_{X_1} - 1\right) SSW_{X_1}} \tag{14}$$

$$SSW_{X_1} = \sum_{h=1}^{L_1} N_h \sigma_h^2 \quad SSW_{X_2} = \sum_{h=1}^{L_2} N_h \sigma_h^2 \tag{15}$$

In the formula, NX_1 and NX_2 represent the number of samples of factors X_1 and X_2, SSW_{X1} and SSW_{X2} are the sum of internal variances after stratification of factors X_1 and X_2, and L_1 and L_2 represent the number of stratification of factors X_1 and X_2.

3.2 Spatio-temporal simulation of vegetation community diversity

The spatiotemporal simulation of vegetation community diversity depends on the deep coupling of multi-source data fusion and ecological model, and its core lies in constructing a computational framework that can reflect the dynamic relationship between environmental gradient and biological response. Taking the Henan section of the Yellow River Basin as the object, this study integrated the vegetation functional parameters (such as NDVI, leaf area index) retrieved by remote sensing and the species distribution data from the ground survey and established a spatially explicit vegetation dynamic simulation system through the collaboration of MaxEnt species distribution model and CLM ecosystem process model. The input layer of the model covers multi-dimensional variables such as climatic elements (temperature, precipitation), topographic attributes (elevation, slope, aspect), soil physical and chemical properties (organic matter content, texture type) and human activity intensity (land use type, night lighting index). With the help of spatial interpolation and scale conversion technology, the data with different resolutions are unified into 1 km × 1 km grid cells to ensure the spatial comparability of environmental driving factors.

The nonlinear response of vegetation functional traits and environmental factors is emphatically solved in model parameterisation. The importance of variables was ranked by random forest algorithm, and the dominant factors affecting the spatial differentiation of vegetation diversity were screened out. For example, the annual average temperature, precipitation seasonal index and soil available water content were identified as the key control variables of the climate-soil dimension. At the same time, the topographic humidity index (TWI) and the gradient of human disturbance intensity were introduced to quantify the effect of landforms on water redistribution and the superposition effect of human activities on habitat fragmentation. In order to describe the succession process of vegetation community, the model uses a dynamic vegetation module to simulate the competitive relationship between dominant species and associated species and combines the time series data of vegetation coverage obtained by remote sensing to calibrate the species niche width and environmental adaptation threshold, thus enhancing the model's ability to explain the dynamic changes of community composition.

The expression of spatial heterogeneity is a technical difficulty in simulation realisation. A stratified random sampling strategy was used to divide ecological units according to landform types (mountains, hills, plains) and land use intensity (high, medium, and low), and sub-models were trained to capture vegetation response mechanisms under different habitat conditions. Aiming at the unique riparian ecological interface of the Henan section of the Yellow River Basin, a buffer-specific parameter set was constructed, and the soil water stress function was modified by the hydrological connectivity index to improve the simulation accuracy of the dynamics of the ecotone between wetland vegetation and xerophytic communities by the model. The model deals with the asynchronous interference between climate change and human activities through the time-step adaptive adjustment mechanism and embeds the interannual climate fluctuation and month-to-month land use change data into the simulation cycle to realise the time-varying coupling of vegetation dynamics and driving factors.

By identifying typical drought years during the research period and comparing the differences in vegetation community diversity indices between drought years and normal years, it was found that drought events led to a significant decrease in NDVI, an average decrease of 15% -30% in community alpha diversity, and more sensitive responses in the herbaceous and shrub layers; At the same time, Mann Kendall trend test and sliding t-test were used to analyse the abrupt changes in diversity before and after extreme climate events. The results showed that drought years often become turning points in diversity patterns, and some regions show irreversible degradation trends. In addition, by constructing a multiple regression model to quantify the response relationship between drought intensity (such as SPI index) and diversity indicators, it was found that when SPI $\leq$ -1.5, the decline in diversity increased exponentially, indicating that vegetation in the Henan section of the Yellow River Basin has a significant threshold response mechanism to extreme drought.

Although the MaxEnt model can effectively simulate species distribution, its results are highly sensitive to sampling bias in species distribution points, and the actual vegetation conditions in some remote areas or areas with high human activity may not be fully captured. In terms of variable selection, although multidimensional environmental factors are integrated, the lack of key driving factors such as soil microbial characteristics and historical disturbances may still lead to incomplete explanations of the recovery mechanism. In addition, there are limitations to the spatiotemporal transferability of models, especially when using models constructed based on the current time period for dynamic recovery process deduction or future climate scenario prediction, extra caution is required. These limitations mean that the explanation for the differences in restoration between western mountainous areas and eastern plains is more presented as a probabilistic framework based on existing data and assumptions, rather than deterministic conclusions.

By comparing the implementation differences between ecological restoration projects in the mountainous areas of western Henan and the plains of eastern Henan, this study delves into the core mechanisms underlying the spatial heterogeneity of vegetation recovery effects: In the western mountains, where natural recovery predominates, the restoration process and outcomes are profoundly constrained by topographical conditions. For instance, steep slopes exhibit slower recovery rates due to poor soil water and nutrient conditions. Despite higher levels of human intervention in the eastern plains, extremely high land use intensity and habitat fragmentation create a weak foundation for ecological recovery, posing greater challenges to stability. Furthermore, the water-heat climate gradient traversing the study area further regulates the recovery potential and succession direction of vegetation communities across different regions, collectively shaping the spatiotemporal pattern of vegetation diversity in the Henan section of the Yellow River basin characterised by “stability in the west and difficulty in the east”.

3.3 Construction of evaluation matrix method

The standard selection is based on the integrity of the ecosystem, and six key indicators have been selected from three core dimensions: biodiversity, ecosystem function, and landscape pattern, aiming to comprehensively reflect the composition, function, and spatial configuration characteristics of vegetation communities.

In terms of indicator processing, the range method was used to normalise each indicator and convert them uniformly to the 0–1 interval, in order to eliminate the differences in dimensionality and numerical range of the original data. Among them, indicators that contribute positively to ecological restoration, such as species richness, are positively normalised, while indicators that indicate negatively to restoration are negatively normalised. Subsequently, based on the weights determined by the Analytic Hierarchy Process (AHP), spatial weighted overlay analysis was performed to generate a comprehensive evaluation map in the GIS platform, which intuitively revealed the spatial differentiation pattern of vegetation restoration status.

Regarding the applicability conditions of the evaluation matrix, this method is particularly suitable for mesoscale regional evaluation, requiring input data to have spatial continuity or reliable spatial interpolation. The premise of its analysis is that there is no severe non-stationary interference during the evaluation period, to ensure that the results reflect a long-term recovery trend rather than short-term fluctuations. When comparing the western mountainous areas with the eastern plains, attention should be paid to the universality of the indicator system for different geomorphic units and ecological processes; If there is a significant difference in the dominant mechanisms between the two places, zoning modelling or adjusting weights can be used to improve the ecological rationality of the evaluation.

3.4 Experiment and results analysis

Table 1 shows that the results obtained by the CA-Markov and MCE-CA-Markov methods in the 2030 NDVI grade forecast are very close. The predicted values of low-grade areas are the same, and there is no difference in proportion. The difference between the predicted values of the middle and low-grade areas is only 0.2 km^2, and the difference in proportion is very small. The difference in the predicted area value of the medium-grade area is 2.7 km^2, accounting for 0.01%. The difference in predicted area values of middle and high-grade areas is 0.2 km^2, and the difference in proportion is also 0.01%.

Table 1 Comparison of predicted values of NDVI grades

NDVI Grade	*CA-Markov model prediction*		*MCE-CA-Markov model prediction*		*Proportion difference (%)*
	Area (km^2)	*Proportion (%)*	*Area (km^2)*	*Proportion (%)*	
Low grade	3.6	0.0	3.6	0.0	0.00
Low-medium grade	217.5	0.6	217.7	0.6	0.00
Medium grade	1056.9	2.7	1059.7	2.7	0.01
Medium-high grade	14,386.6	36.5	14,386.4	36.5	0.00
Higher grade	24,490.3	62.2	24,487.7	62.2	0.01

Using the raster calculator of ArcGIS, spatiotemporal changes in ecosystem services from 1990 to 2020 were assessed. As shown in Figure 4, a high value indicates a strong function, and vice versa. The water conservation capacity weakened in the north and increased in the south, and the maximum value decreased by 67%. Soil conservation capacity generally improved, with a maximum decrease of 96.1% in the north and south.

Figure 4 Interannual variation of ecosystem services (see online version for colours)

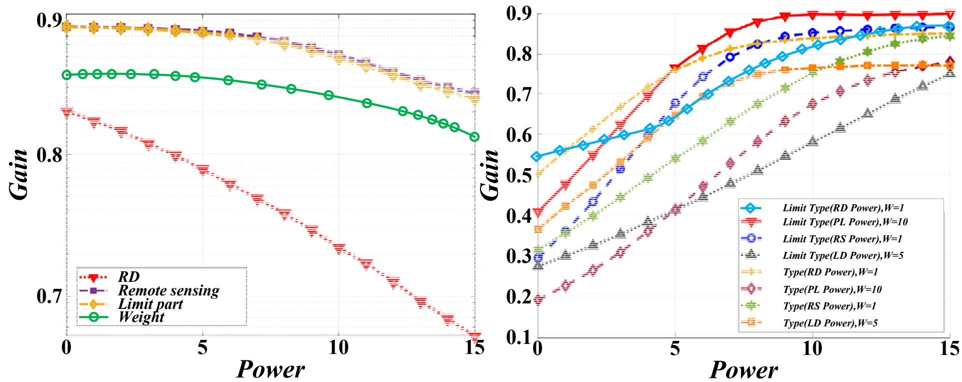

Figure 5 Changes in synergistic trade-offs of ecosystem services (see online version for colours)

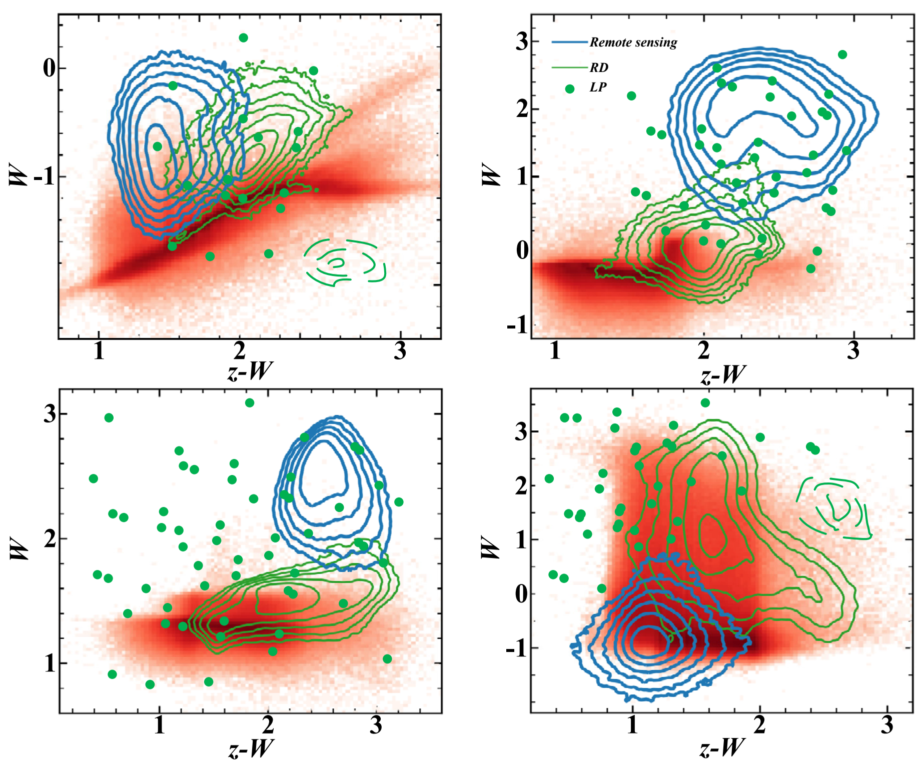

Bivariate autocorrelation analysis was used to explore the spatial trade-off and synergistic relationship of ecosystem services around the Yellow River at three scales of 10 km^2, 150 km^2 and 900 km^2, and their spatial and temporal distribution patterns were revealed.

Results Figure 5 shows that the spatial trade-offs and synergy effects of ecosystem services are unevenly distributed at the three scales.

Figure 6 Synergistic and trade-off area proportion distribution at different scales (see online version for colours)

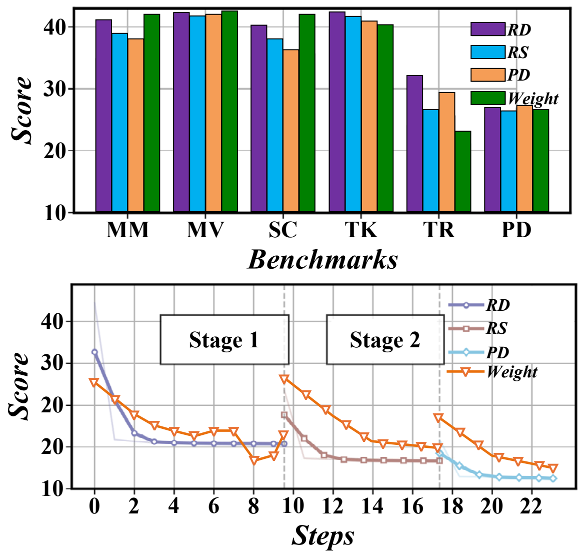

Figure 7 Coefficient of variation of hyperspectral reflectance with different spatial resolutions (see online version for colours)

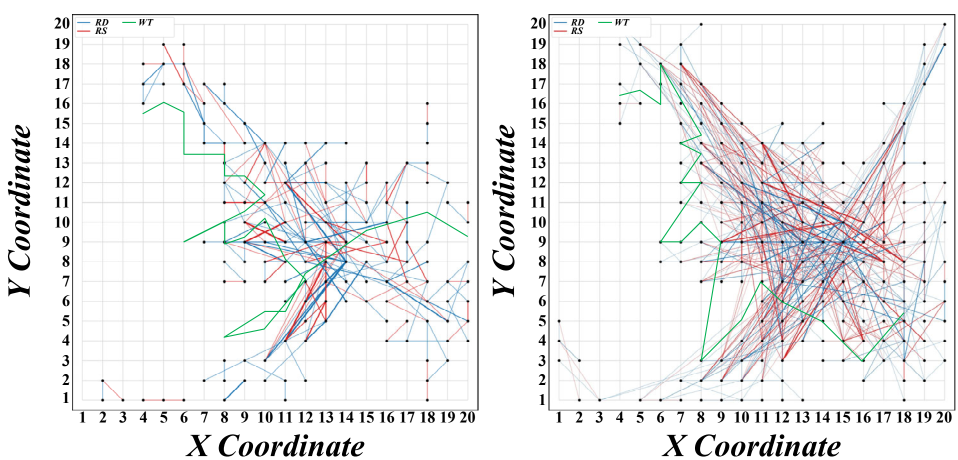

As shown in Figure 6, OM identified seven ecosystem service clusters on three scales and demonstrated their transitions in the Yellow River Rim region. From 1990 to 2000, the area of B1, B4 and B6 expanded, while the area of B2, B3, B5 and B7 decreased, especially the change from B2 to B1, B4 and B6 was significant. From 2000 to 2010, B1, B2, B3 and B6 continued to expand, B4, B5 and B7 shrank, and B4 changed significantly to B1 and B2. From 2010 to 2020, B1, B3, B5 and B7 increased, while B2, B4 and B6 decreased. B2 changed significantly to multiple clusters, while B3 and B7 did not change.

Figure 7 shows that the average reflectivity variation coefficient of the UAV hyperspectrum decreases as the resolution increases from 0.1 meters to 1 meter and also shows a weakening trend as the resolution increases from 5 meters to 20 meters. This is consistent with multispectral data variation, with spectral coefficients of variation higher at 5 m resolution than at 1 m resolution. The coefficient of variation of hyperspectral reflectance of different grassland types at different resolutions and bands is significantly different.

Looking at the data in Table 2, the medium-high and high vegetation coverage areas accounted for 13.52% and 61.09% respectively. The spatial distribution showed that the annual maximum FVC mean was high peripherally and low in the centre.

Table 2 Statistics of FVC area of different grades

FVC rating	*Area (km2)*	*Specific gravity (%)*
Low	2,519.76	12.51
Medium low	1,115.50	5.54
medium	1,583.34	7.85
Medium high	2,779.57	13.79
High	12,556.56	62.31

Figure 8 Annual changes of vegetation coverage of different grades (see online version for colours)

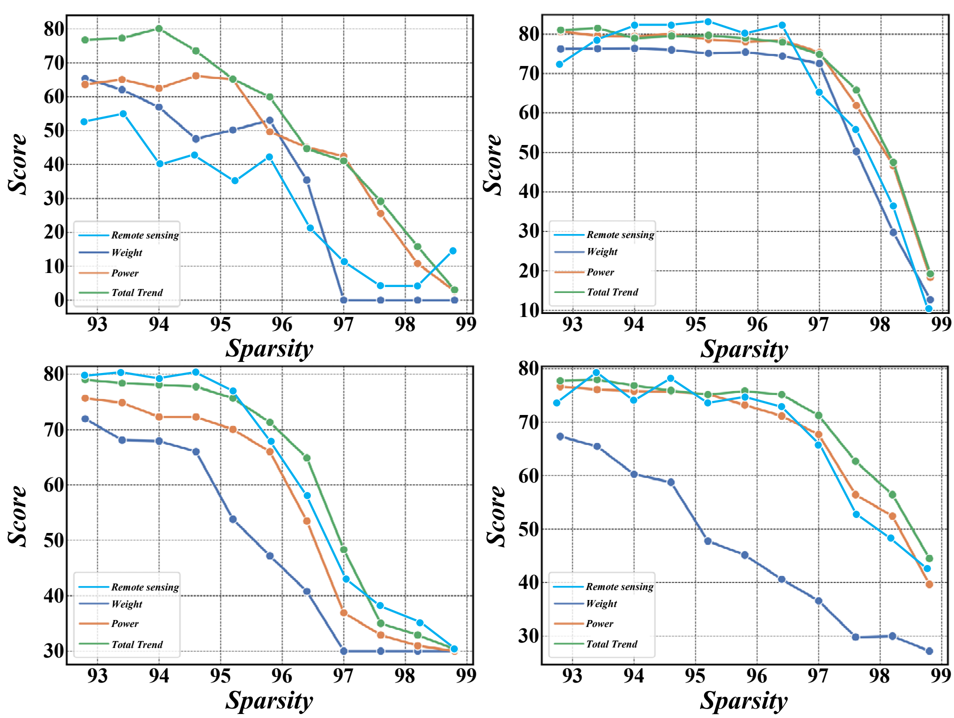

The distribution of vegetation coverage levels in different years was analysed (see Figure 8), and the results showed that the area proportion of low to medium-high FVC areas fluctuated and increased. In contrast, the opposite was true in high FVC areas. From 2000 to 2015, the proportion of high FVC areas exceeded 55% and dropped to less than 50% in 2020; The area ratio of medium and high FVC areas is maintained at 5%–9%; The proportion of medium and low FVC areas was the highest in 2020 and the lowest in 2000, with a change of no more than 3%; The area proportion of low FVC areas fluctuates between 13% and 18%, with the lowest in 2015 and the highest in 2020.

Table 3 shows that the distribution proportion of vegetation phenology at different heights in mountainous areas is different. The results showed that the proportion of cultivated land decreased with the increase of height, and the proportion of forest increased. The proportion of grassland and shrubs increased first and then decreased, and the proportion of grassland was the highest in the middle altitude zone.

Table 3 Proportion of vegetation types of vegetation phenology at different elevations

Altitude zoning	*Altitude range (m)*	*Proportion of cultivated land (%)*	*Forest share (%)*	*Shrubs (%)*	*Proportion of grassland (%)*
Low altitude	≤500	83.6	18.2	0.0	0.2
Medium and low altitude	500–1,000	34.2	58.8	0.1	9.0
Middle altitude	1,000–1,500	9.8	65.6	0.1	26.5
Medium and high altitude	1,500–2,000	0.9	92.7	0.0	8.4
High altitude	>2,000	0.0	98.7	0.0	3.3

As shown in Figure 9, the growth cycle of farmland fluctuates greatly, and the overall growth cycle is slightly extended, increasing by 0.5 days every decade. The longest cycle was 185 days in 2004 and 2008; It was the shortest in 2010, with 166 days. The average period is 177 days, with 10 out of 20 years exceeding the average and 2 years being equal to the average.

Figure 9 Change trend chart of growth period length (see online version for colours)

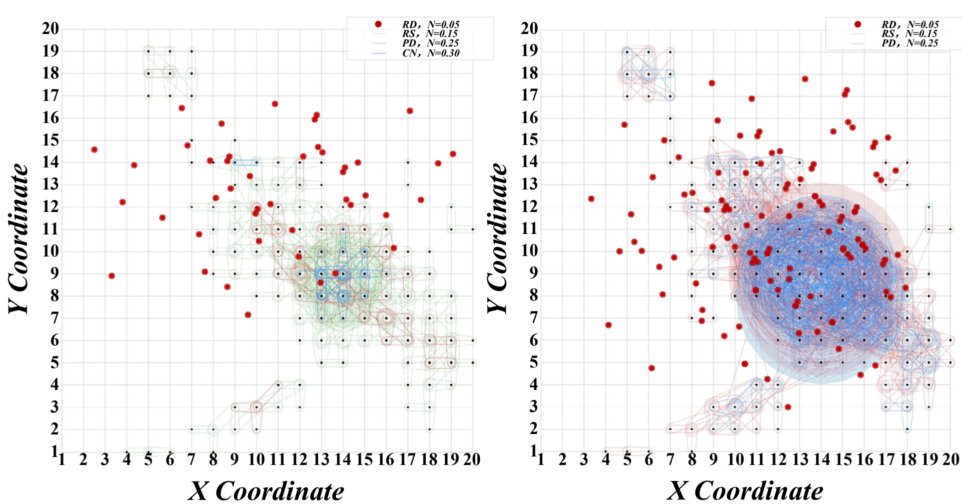

By constructing a vegetation diversity index system, the dynamic evolution of vegetation community structure in the Henan section of the Yellow River Basin from 2000 to 2022 was systematically analysed. Overall, the vegetation coverage (NDVI mean) in the study area showed a significant upward trend, with an average annual growth rate of 0.012 ($p < 0.01$). However, vegetation diversity indicators exhibit more complex temporal variations (Table 4). The species richness increased rapidly in the early stages of ecological engineering implementation (2000–2010), with a cumulative increase of over 28%, but the growth rate slowed down in the later stages; The Shannon diversity index and Pielou evenness index have shown a slow downward trend since 2010, reflecting a possible simplification trend in community structure as coverage increases. These temporal changes are closely related to the evolution of climate fluctuations, ecological engineering stages, and human disturbance intensity. Especially after 2010, the dominance of trees in artificial afforestation areas increased, resulting in a decrease in understory species richness and community uniformity, highlighting the asynchronous growth of quantity and quality improvement in vegetation restoration. Time series analysis further reveals that autumn temperature fluctuations have a strong explanatory power for the annual variation of diversity indicators ($R^2 = 0.58$), while NDVI is mainly controlled by spring precipitation, indicating significant seasonal differences and lag effects in the impact of climate driving factors on different vegetation attributes.

This study reconstructs long-term NDVI time series based on multi-source remote sensing data to analyse vegetation dynamics. Differences in spectral characteristics and spatiotemporal resolution among sensors may induce systematic biases in NDVI values, particularly pronounced in vegetation transition zones. Errors from preprocessing steps such as atmospheric correction and cloud masking are more likely to accumulate in the climatically dynamic Henan region, thereby interfering with the accurate identification of trend signals and the assessment of ecological engineering effectiveness. Therefore, when conducting attribution analyses of vegetation restoration differences between western mountainous areas and eastern plains, it is essential to fully account for this data uncertainty. Considering the phenological dynamics of vegetation in the study area, the temporal stability of vegetation growth processes can also provide supplementary reference for data interpretation.

Table 4 Ecological indicator change data

Year	*Average NDVI*	*Species richness index*	*Shannon diversity index*	*Pielou evenness index*	*Main driving factor (notes)*
2000	0.42	12.30	2.15	0.78	Initial stage of grain for green project
2005	0.48	14.50	2.34	0.81	Effective period of ecological engineering
2010	0.52	15.80	2.41	0.79	Impact of precipitation fluctuations
2015	0.55	16.20	2.38	0.76	Emergence of monoculture plantations
2020	0.58	16.50	2.35	0.75	Climate warming and drying trend
2022	0.59	16.70	2.33	0.74	Slowing recovery rate

From 2002 to 2021, the daily change of growth termination was more stable than that of growth start (see Figure 10), with a coefficient of variation ranging from 0% to 20.48%. The coefficient of variation of 45.72% pixels is less than 1%, and the distribution is concentrated, indicating that the fluctuation of growth termination day is stable. Pixel points with coefficient of variation of 1% to 2% and 2% to 3% accounted for 32.39% and 10.41%, respectively, and were widely distributed from upstream to downstream.

Figure 10 Spatial distribution of spatial coefficient of variation on the beginning day of growth period (see online version for colours)

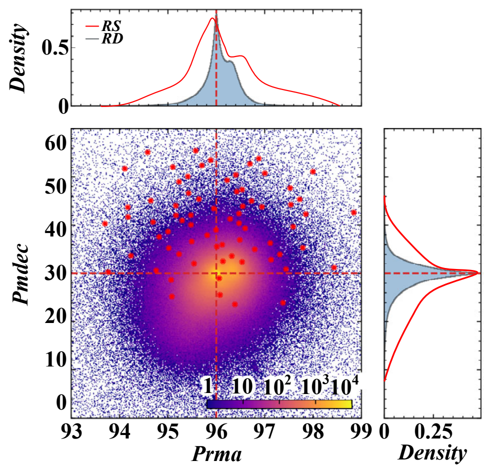

4 Discussion

This study utilised soil salinisation remote sensing inversion products, historical distribution maps of saline-alkali land, groundwater monitoring data, as well as vector data of mining boundaries and activity intensities as auxiliary data sources to verify the spatial and temporal distribution patterns of vegetation community diversity affected by soil salinisation and mining activities in the Yellow River section of Henan Province.

Using NDVI annual growth rate below 0.005 as the criterion for vegetation degradation or growth stagnation, and landscape disturbance intensity index above 0.7 as the indicator of severe habitat degradation caused by human activities. These two threshold settings are based on regional specific ecology, combined with the arid semi-arid climate background, main vegetation growth rhythms, and historical long-term observation data in the Yellow River Basin, to ensure their representativeness of local ecological processes; The second is to obtain statistical support for sensitivity analysis, and by adjusting the threshold, verify that the model under this setting responds significantly and stably to key interference factors such as soil salinisation and mining, and can effectively separate signals of sustained degradation caused by human activities.

The Shannon index of the natural restoration area (shrub and herbaceous community) is 2.85 ± 0.23, and the Pielou index is 0.78 ± 0.05, showing a significant positive correlation between the two ($r = 0.67$, $p<0.01$), indicating a synergistic increase in species diversity and evenness during the natural restoration process, and the community structure tends to stabilise. The Shannon index of the artificial forest area is 1.92 ± 0.31, and the Pielou index is 0.62 ± 0.08. The correlation between the two is weak ($r = 0.28$, $p > 0.05$), and the evenness is significantly lower than that of the natural restoration area ($p < 0.01$), reflecting the obvious dominance of dominant species and uneven distribution of species in the artificial forest community. By constructing a two-dimensional discriminant space of diversity uniformity, natural restoration sample points are mainly clustered in the high diversity high uniformity quadrant (accounting for 72.3% of the sample size), while artificial forest sample points are dispersed in the low uniformity region (68.5% of low uniformity samples). There is a significant separation in the distribution of the two in the discriminant space (MANOVA test, $p<0.001$). This differential pattern further validates the ecological effects of different restoration approaches in ecological engineering: natural restoration is more conducive to forming structurally stable and evenly distributed communities, while artificial forest construction can rapidly increase vegetation coverage, but may lead to a single community structure. This analysis provides a more refined discrimination basis for the evaluation of ecological engineering effects from the perspective of community structure and function, and strengthens the comparability of ecological effects of different restoration models.

After adjusting the combination of parameters such as the number of trees, maximum number of features, and maximum depth, the ranking of the core driving factors remains stable. The importance ranking of climate factors (annual average temperature, precipitation) remains unchanged in 95% of parameter combinations (ranking fluctuation ≤ 1), with a coefficient of variation of 0.08-0.12. The ranking of terrain and soil factors is stable (fluctuation ≤ 2) in 85% of parameter combinations, with a coefficient of variation of 0.15-0.20. The stability of the ranking of human activity factors is relatively low (fluctuation ≤ 2 in 75% of combinations), with a coefficient of variation of 0.22–0.28. The Kendall consistency coefficient is 0.89 ($p<0.001$), and the confidence interval widths for importance scores under Bootstrap resampling are all less than 0.05. The results indicate that the random forest model has high consistency in ranking the importance of driving factors under different parameter settings, supporting its reliability in this study.

5 Conclusions

By integrating multi-source remote sensing data and ecological models, this study systematically revealed the temporal and spatial evolution characteristics and driving mechanisms of vegetation community diversity in the Henan section of the Yellow River Basin from 2000 to 2022.

1 The vegetation coverage (NDVI) extracted based on Landsat and MODIS time series data shows that the average NDVI in the study area shows a significant upward trend as a whole (average annual growth rate 0.012, $p < 0.01$). However, the spatial heterogeneity is prominent: the growth rate of NDVI in mountainous areas such as Funiu Mountain and Xionger Mountain in the west is 0.018/year, while that in the eastern Yellow Pan Plain is only 0.008/year, indicating that the dual effects of topography and human activities have a profound impact on the vegetation restoration rate. Through the coupling simulation of the MaxEnt model and CLM model, it is found that the contribution rate of climate factors (annual average temperature and precipitation) to the explanation of vegetation spatial pattern is 48.3%. In comparison, the combined contribution of topographic undulation and soil

organic matter content is 31.7%, highlighting the basic role of physical geography elements in vegetation differentiation. Due to cultivated land expansion and urbanisation encroachment in the 5-kilometre buffer zone along the Yellow River, the natural vegetation area decreased by 23.6% compared with 2000. The human activity intensity index and vegetation diversity index (Shannon index) showed a significant negative correlation ($R^2 = 0.67$), revealing the persistent stress of high-intensity development on riparian ecological corridors.

2 There is a significant spatial differentiation in the vegetation restoration effect in the ecological engineering implementation area. By returning farmland to forests, the richness of shrub and herbaceous communities in the loess hilly area of western Henan has increased by 14.2%; However, in the artificial forest planting area, due to the increase in tree dominance, the number of understory species decreased by 8.5%, reflecting that single vegetation reconstruction may weaken community stability. Seasonal scale analysis further reveals that NDVI has the highest sensitivity to spring precipitation changes (regression coefficient $\beta = 0.76$), but there is a fluctuation of $\pm$ 0.12 in this coefficient between different climate years, indicating that seasonal water and heat allocation will affect sensitivity intensity; Vegetation diversity is more sensitive to temperature fluctuations in autumn ($\beta = 0.63$), and its uncertainty mainly comes from the influence of interannual temperature fluctuations and extreme climate events. This result highlights the significant phenological differences in the driving force of climate change on vegetation dynamics, and the seasonal sensitivity is modulated by both climate fluctuations and human intervention.

3 Through the quantitative decoupling of multi-factor contribution by random forest algorithm, it is found that the direct impact of human disturbance on community succession accounts for 20.5%, among which soil salinisation caused by cultivated land irrigation increases the proportion of salt-tolerant plants in the Yellow River beach area by 19.3%, while the vegetation fragmentation index (PD) within 10 kilometres around the mining area increases by 37.6%, which confirms the differentiated shaping mechanism of different human activity types on vegetation patterns.

4 The global Moran's I analysis (Moran's I of NDVI sequences from 2000 to 2022 ranged from 0.32 to 0.48, $p < 0.01$) indicates a significant spatial positive correlation in vegetation coverage.

Further analysis of Getis-Ord Gi* hotspots identified the western mountainous region as a consistently high-value hotspot area ($Z > 2.58$, $p < 0.01$), while the eastern plain and the urban belt along the Yellow River were identified as low value cold spots ($Z < -1.96$, $p < 0.05$). This spatial differentiation pattern is consistent with the terrain gradient and human activity intensity distribution. The spatial statistical results not only verify the non-randomness of vegetation patterns, but also provide a quantitative basis for explaining that the NDVI growth rate in the western region (0.018/year) is significantly higher than that in the eastern region (0.008/year), indicating that ecological restoration hotspots and human disturbance cold spots jointly drive the differential evolution of vegetation.

This study achieved a collaborative analysis of multi-scale environmental factors and vegetation dynamics in the Henan section of the Yellow River Basin by constructing a technical framework of "remote sensing inversion model simulation driven analysis".

The results showed that vegetation restoration was both effective and challenging. In response to the high natural recovery potential (NDVI annual growth rate of 0.018) in western mountainous areas, protection and natural restoration should be the main focus, and the connectivity protection of ecological hotspots such as Funiu Mountain and Xiong'er Mountain should be strengthened. Mineral development and slope cultivation should be restricted to promote positive succession of forest communities; For the eastern plain, especially the yellow buffer zone and surrounding urban areas with NDVI annual growth rates below 0.005, ecological reconstruction led by human intervention should be implemented, and a composite vegetation corridor should be constructed along the riverbank. Ecological control red lines should be strictly delineated in areas with human activity intensity above 0.7, and targeted restoration of salt and drought tolerant local vegetation should be carried out. The evaluation matrix of "natural restoration potential artificial intervention priority" proposed in the study can provide spatially clear decision support for ecological management of watershed zoning and classification.

Funding

This work was supported by Scientific and Technological Research Project of Henan Province (232102320055), Natural Science Foundation of Henan (242300420493 and 232300420455), Fundamental Research Fund of Henan Academy of Sciences (230601069 and 20250601013), High level Achievement Award and Cultivation Project of Henan Academy of Sciences (20252301003 and 20252301006).

Declarations

The authors declare that they have no known competing financial interests or personal relationships that could have appeared to influence the work reported in this paper.

References

Bai, T., Wang, X-S. and Han, P-F. (2024) 'Controls of groundwater-dependent vegetation coverage in the yellow river basin, china: insights from interpretable machine learning', *Journal of Hydrology*, Vol. 631, No. 11, Art. No. 130747, DOI: 10.1016/j.jhydrol.2024.130747.

Bhatt, P. and Maclean, A.L. (2023) 'Comparison of high-resolution NAIP and unmanned aerial vehicle (UAV) imagery for natural vegetation community's classification using machine learning approaches', *Gscience & Remote Sensing*, Vol. 60, No. 1, Art. No. 2177448, DOI: 10.1080/15481603.2023.2177448.

Chai, H., Zhao, Y., Xu, H., Xu, M., Li, W., Chen, L. and Wang, Z. (2024) 'Analysis of ecological environment in the Shanxi section of the Yellow River Basin and coal mining area based on improved remote sensing ecological index', *Sensors*, Vol. 24, No. 20, p.6560, DOI: 10.3390/s24206560.

Chen, X., Huang, Q., Xiong, Y., Yang, Q., Li, H., Hou, Z. and Huang, G. (2023a) 'Tracking the spatio-temporal change of the main food crop planting structure in the Yellow River Basin over 2001-2020', *Computers and Electronics in Agriculture*, Vol. 212, No.2, Art. No. 108102, DOI: 10.1016/j.compag.2023.108102.

Chen, Y., Cui, C., Han, Z., Liu, F., Wu, Q. and Yu, W. (2023b) 'Identifying spatiotemporal patterns of multiscale connectivity in the flow space of urban agglomeration in the Yellow River Basin', *ISPRS International Journal of Geo-Information*, Vol. 12, No. 11, p.447, DOI:10.3390/ijgi12110447.

Chen, Z., Liu, X., Feng, H., Wang, H. and Hao, C. (2024) 'The spatiotemporal evolution of vegetation in the Henan section of the Yellow River Basin and mining areas based on the normalized difference vegetation index', *Remote Sensing*, Vol. 16, No. 23, p.4419, DOI:10.3390/rs16234419.

Chi, W., Wang, Y., Lou, Y., Na, Y. and Luo, Q. (2022) 'Effect of land use/cover change on soil wind erosion in the Yellow River Basin since the 1990s', *Sustainability*, Vol. 14, No. 19, p.12930, DOI:10.3390/su141912930.

Ci, F., Wang, Z. and Hu, Q. (2024) 'Spatial pattern characteristics and optimization policies of low-carbon innovation levels in the urban agglomerations in the Yellow River Basin', *Journal of Cleaner Production*, Vol. 439, No. 9, Art. No. 140856, DOI: 10.1016/j.jclepro.2024.140856.

Cui, Y., Li, L., Lei, Y. and Wu, S. (2024) 'The performance and influencing factors of high-quality development of resource-based cities in the Yellow River basin under reducing pollution and carbon emissions constraints', *Resources Policy*, Vol. 88, No. 1, Art. No. 104488, DOI: 10.1016/j.resourpol.2023.104488.

Dai, Q., Cui, C-F. and Wang, S. (2022) 'Spatiotemporal variation and sustainability of NDVI in the Yellow River basin', *Irrigation and Drainage*, Vol. 71, No. 5, pp.1304–1318.

Duan, Y., Zhao, H., Zhang, H., Qin, Y. and Han, Z. (2022) 'The spatiotemporal effects and drivers of industrial agglomeration – a case study of counties in the Yellow River basin', *Frontiers in Environmental Science*, Vol. 10, DOI: 10.3389/fenvs.2022.982904.

Feng, D., Han, J., Jia, H., Chang, X., Guo, J. and Huang, P. (2023a) 'Regional economic growth and environmental protection in China: the Yellow River Basin economic zone as an example', *Sustainability*, Vol. 15, No. 14, p.10790, DOI: 10.3390/su151410790.

Feng, Y., Huang, C., Song, X., and Gu, J. (2023b) 'Assessing progress and interactions toward SDG 11 indicators based on geospatial big data at prefecture-level cities in the yellow river basin between 2015 and 2020', *Remote Sensing*, Vol. 15, No. 6, p.1668, DOI: 10.3390/rs15061668.

Feng, R. and Qu, X. (2023) 'Innovation-driven industrial agglomeration impact on green economic growth in the Yellow River basin: an empirical analysis', *Sustainability*, Vol. 15, No. 17, p.13264, DOI:10.3390/su151713264.

Fernandez-Guisuraga, J.M., Calvo, L., Quintano, C., Fernandez-Manso, A. and Fernandes, P.M. (2023) 'Fractional vegetation cover ratio estimated from radiative transfer modeling outperforms spectral indices to assess fire severity in several Mediterranean plant communities', *Remote Sensing of Environment*, Vol. 290, Art. No. 113542, DOI: 10.1016/j.rse.2023.113542.

Han, X., Hua, E., Guan, J., Engel, B.A., Liu, R., Bai, Y., Sun, S. and Wang, Y. (2024) 'Development of a method to assess synergy and competition for water use among water-energy-food nexus in the Yellow River basin: water quantity-quality dimensions', *Journal of Hydrology*, Vol. 639, No. 5, Art. No. 131607, DOI: 10.1016/j.jhydrol.2024.131607.

Hou, Y., Ma, Y., Hou, Z., Arif, M., Li, J., Ming, X., Liu, X. and Xing, Q. (2024) 'Space-ground remote sensor network for monitoring suspended sediments in the Yellow River Basin', *Sensors*, Vol. 24, No. 21, p.6888, DOI: 10.3390/s24216888.

Muentes, J., Moreira, J. M., Chata, C., Alcivar, A., Zorrilla, I. and Salas-Macias, C.A. (2024) 'Characterization of the vegetation community and its contribution to a carbon stock in a dry forest', *Enfoque Ute*, Vol. 15, No. 2, pp.1–8.

Qin, Y., Li, Z., Ding, J., Zhao, F. and Meng, M. (2023) 'Automatic optimization model of transmission line based on GIS and genetic algorithm', *Array*, Vol. 17, No.2, Art. No. 100266, DOI: 10.1016/j.array.2022.100266.

Sharma, R.C. (2022) ‘An ultra-resolution features extraction suite for community-level vegetation differentiation and mapping at a sub-meter resolution’, *Remote Sensing*, Vol. 14, No. 13, p.3145, DOI: 10.3390/rs14133145.

Shi, J., Pan, Z., Jiang, L., and Zhai, X. (2023) ‘An ontology-based methodology to establish city information model of digital twin city by merging BIM, GIS and IoT’, *Advanced Engineering Informatics*, Vol. 57, No. 4, Art. No. 102114, DOI: 10.1016/j.aei.2023.102114.

Tang, X., Wei, T., He, Y. and He, K. (2022) ‘Differentiation of vegetation community characteristics by altitude within urban parks and their service functions in a semi-arid mountain valley: a case study of Lanzhou City’, *ISPRS International Journal of Geo-Information*, Vol. 11, No. 11, p.549, DOI:10.3390/ijgi11110549.

van Deventer, H., Linstrom, A., Naidoo, L., Job, N., Sieben, E.J.J. and Cho, M.A. (2022) ‘Comparison between Sentinel-2 and WorldView-3 sensors in mapping wetland vegetation communities of the Grassland Biome of South Africa, for monitoring under climate change’, *Remote Sensing Applications-Society and Environment*, Vol. 28, No. 24, Art. No. 100875, DOI: 10.1016/j.rsase.2022.100875.

Wang, C., Pavelsky, T.M., Kyzivat, E.D., Garcia-Tigreros, F., Podest, E., Yao, F., Yang, X., Zhang, S., Song, C., Langhorst, T., Dolan, W., Kurek, M.R., Harlan, M.E., Smith, L.C., Butman, D.E., Spencer, R.G.M., Gleason, C.J., Wickland, K.P., Striegl, R.G. and Peters, D.L. (2023) ‘Quantification of wetland vegetation communities features with airborne AVIRIS-NG, UAVSAR, and UAV LiDAR data in Peace-Athabasca Delta’, *Remote Sensing of Environment*, Vol. 294, Art. No. 113646, DOI: 10.1016/j.rse.2023.113646.

Wang, L., Wu, Z., Zhang, W., Wang, X. and Feng, W. (2025) ‘Dynamic life cycle environmental impact assessment for urban built environment based on BIM and GIS’, *Energy and Buildings*, Vol. 333, Art. No. 115445, DOI: 10.1016/j.enbuild.2025.115445.

Wilkho, R.S., Gharaibeh, N.G. and Chang, S. (2025) ‘A GIS-based tool for dynamic assessment of community susceptibility to flash flooding’, *Journal of Flood Risk Management*, Vol. 18, No. 1, p.e13049, DOI: 10.1111/jfr3.13049.

Zavari, M., Shahhosseini, V., Ardeshir, A., and Sebt, M.H. (2022) ‘Multi-objective optimization of dynamic construction site layout using BIM and GIS’, *Journal of Building Engineering*, Vol. 52, No. 4, Art. No. 104518, DOI: 10.1016/j.jobe.2022.104518.

Zhang, T., Bi, Y., Zhu, X. and Gao, X. (2023) ‘Identification and classification of small sample desert grassland vegetation communities based on dynamic graph convolution and UAV hyperspectral imagery’, *Sensors*, Vol. 23, No. 5, p.2856, DOI: 10.3390/s23052856.

Zhao, Z., Zhang, M., Chen, J., Qu, T. and Huang, G.Q. (2022) ‘Digital twin-enabled dynamic spatial-temporal knowledge graph for production logistics resource allocation’, *Computers & Industrial Engineering*, Vol. 171, No. 17, Art. No. 108454, DOI: 0.1016/j.cie.2022.108454.

Zhu, Z., Wang, H., Yang, Z., Huai, W., Huang, D. and Chen, X. (2024) ‘Landscape pattern changes of aquatic vegetation communities and their response to hydrological processes in Poyang Lake, China’, *Water*, Vol. 16, No. 11, p.1482, DOI: 10.3390/w16111482.